

PAPER • OPEN ACCESS

Revolutionizing plasmonic platform via magnetic field-assisted confined ultrafast laser deposition of high-density, uniform, and ultrafine nanoparticle arrays


To cite this article: Jin Xu *et al* 2024 *Int. J. Extrem. Manuf.* **6** 035003

View the [article online](#) for updates and enhancements.

You may also like

- [Plasmonic Au nanorods stabilized within anodic aluminum oxide pore channels against high-temperature treatment](#)
Kai Liu, Paul R Ohodnicki, Xiaoqing Kong et al.
- [Gap mode Raman spectroscopy under attenuated total reflection geometry](#)
Keitaro Akai, Chiaki Iida and Masayuki Futamata
- [Anisotropic surface enhanced Raman scattering in nanoparticle and nanowire arrays](#)
Mukesh Ranjan and Stefan Facsko

Revolutionizing plasmonic platform via magnetic field-assisted confined ultrafast laser deposition of high-density, uniform, and ultrafine nanoparticle arrays

Jin Xu¹, Lingfeng Wang^{1,2}, Peilin Yang¹, Haoqing Jiang^{1,2}, Huai Zheng², Licong An¹, Xingtao Liu¹ and Gary J Cheng^{1,*} 

¹ School of Industrial Engineering, Purdue University, West Lafayette, IN 47906, United States of America

² Institute of Technological Sciences, Wuhan University, Wuhan, Hubei 430072, People's Republic of China

E-mail: gjcheng@purdue.edu

Received 26 July 2023, revised 15 October 2023

Accepted for publication 5 March 2024

Published 20 March 2024



CrossMark

Abstract

The remarkable capabilities of 2D plasmonic surfaces in controlling optical waves have garnered significant attention. However, the challenge of large-scale manufacturing of uniform, well-aligned, and tunable plasmonic surfaces has hindered their industrialization. To address this, we present a groundbreaking tunable plasmonic platform design achieved through magnetic field (MF) assisted ultrafast laser direct deposition in air. Through precise control of metal nanoparticles (NPs), with cobalt (Co) serving as the model material, employing an MF, and fine-tuning ultrafast laser parameters, we have effectively converted coarse and non-uniform NPs into densely packed, uniform, and ultrafine NPs (~ 3 nm). This revolutionary advancement results in the creation of customizable plasmonic ‘hot spots,’ which play a pivotal role in surface-enhanced Raman spectroscopy (SERS) sensors. The profound impact of this designable plasmonic platform lies in its close association with plasmonic resonance and energy enhancement. When the plasmonic nanostructures resonate with incident light, they generate intense local electromagnetic fields, thus vastly increasing the Raman scattering signal. This enhancement leads to an outstanding 2–18 fold boost in SERS performance and unparalleled sensing sensitivity down to 10^{-10} M. Notably, the plasmonic platform also demonstrates robustness, retaining its sensing capability even after undergoing 50 cycles of rinsing and re-loading of chemicals. Moreover, this work adheres to green manufacturing standards, making it an efficient and environmentally friendly method for customizing plasmonic ‘hot spots’ in SERS devices. Our study not only achieves the formation of high-density, uniform, and ultrafine NP arrays on a tunable plasmonic platform but also showcases the profound relation between

* Author to whom any correspondence should be addressed.



Original content from this work may be used under the terms of the [Creative Commons Attribution 4.0 licence](https://creativecommons.org/licenses/by/4.0/). Any further distribution of this work must maintain attribution to the author(s) and the title of the work, journal citation and DOI.

plasmonic resonance and energy enhancement. The outstanding results observed in SERS sensors further emphasize the immense potential of this technology for energy-related applications, including photocatalysis, photovoltaics, and clean water, propelling us closer to a sustainable and cleaner future.

Supplementary material for this article is available [online](#)

Keywords: magnetic field manipulation, laser deposition, metasurface, SERS

1. Introduction

Plasmonic surfaces, with their ability to manipulate light at the nanoscale through the arrangement of distributed metallic nanostructures, hold immense significance in various energy research fields [1]. These metallic nanostructures, functioning as nano-antennas on the 2D surfaces, interact with incident light, resulting in the resonant excitation of plasmons and the formation of nanoscale ‘hot spots’ that can modify optical wavefronts [2]. The extraordinary wavefront shaping capabilities of plasmonic surfaces encompass a range of applications, from super-lenses and electromagnetic shielding to optical camouflage, holograms, and surface-enhanced Raman scattering (SERS) platforms [3–9]. Of particular interest is the ability to engineer plasmonic surfaces with precise control over their micro-structural design to achieve desired functionalities. SERS, for example, provides molecular diagnostics through inelastic light scattering by molecular vibrations, offering valuable ‘fingerprint’ information [10–13]. However, the inherent limitation of conventional Raman spectroscopy lies in its low scattering intensity, restricting its applications for chemicals in low concentrations [14–16]. To address this challenge, the SERS technique has been developed, utilizing specially designed metallic patterns with high-curvature nanostructures and gaps to significantly enhance light excitation of surface plasma resonances [17]. The resulting confined electromagnetic fields (EFs) or ‘hot spots’ are believed to originate from localized surface plasmons arising from the coupling of light and surface patterns [18].

Key factors to optimizing SERS performance are the size and compactness of nanoparticles (NPs). Smaller and more compact NPs exhibit stronger plasmonic resonances as their electrons oscillate more readily when subjected to light of specific frequencies. However, achieving tunable nanoscale ‘hot spots’ on a large scale for SERS patterns remains a challenging and insufficiently explored aspect of research. This calls for intensified efforts toward green manufacturing approaches that allow for precise control and scalability of such plasmonic patterns. Considering the vast potential of plasmonic platforms in various energy-related applications, including photocatalysis, photovoltaics, and clean water, it is imperative to deepen our understanding and advance the fabrication techniques of these materials. Emphasizing the controllability of micro-structural design and scalability in plasmonic surfaces will undoubtedly drive significant advancements in energy research, paving the way for sustainable and cleaner technologies.

Laser processing could be an ideal alternative manufacturing technique to overcome these metamaterial fabrication limits. By pulsed laser manufacturing, laser shock peening effects would occur, and metallic nanostructures could be fast imprinted on large-scale with enhanced surface plasma ‘hot spots’ [19, 20]. Liquid metal could also be massively processed using pulsed-laser-induced shockwave [21], with fancily tuned laser spot sizes. Periodical micro-structural liquid metal patterns were synthesized as mechanically strong electric circuits. Thus, laser techniques are able to provide a wide variety of customized solutions by selecting the suitable wavelengths, laser operation mode (pulsed or continuous-wave laser), laser pulse width, laser energy, spot size, and frequency. However, these previous studies were limited to a single material system like aluminum foil or liquid metal. In plasmonic applications like SERS, composite systems are usually more functional to provide abundant plasmonic ‘hot spots’. Considering NP/carbon composites [22, 23], the metal NPs were usually assembled into compact arrays to provide enhanced surface plasmon, while the carbon would serve as a backbone to locate the NP arrays as green and affordable mechanical supports. A discussion of the effect of particle size and its effect on SERS continues to be of interest. The largest SERS enhancement sites are situated in the nanoscale gaps between NP dimers, and analytes adsorbed in these ‘hot spots’ are thought to be responsible for most of the SERS signal [17, 24]. Increasing particle size decreases the final particle coverage, which diminishes the number of hot spots situated in the SERS excitation area and thus decreases the signal [25]. At the nanoscale, the plasmonic resonances of a particle can be strongly influenced by its size and shape, as well as the material it is made of. The plasmonic properties of a particle are also affected by its proximity to other particles. When particles are close together, their plasmons can interact with each other, leading to additional resonances and new behavior. Sub-3 nm NPs with a close and compact arrangement would have superior plasmonic properties compared to larger or more dispersed particles. This is because the small size of the particles and the close proximity between them lead to stronger plasmonic resonances, which can result in enhanced optical absorption and scattering of light. Additionally, the close arrangement of the particles can result in novel optical phenomena, such as localized surface plasmon resonances, that are not observed in larger or more dispersed particles. Overall, the superior plasmonic properties of sub-3 nm NPs with a close and compact arrangement would be one of the best choice to serve as metal NP/carbon composite SERS devices.

Paramagnetic NPs can be aligned using a magnetic field (MF) by exploiting the magnetic dipole moment of the particles. Paramagnetic NPs have a magnetic moment due to their internal magnetic structure when interacts with an external MF. When an MF is applied, the magnetic moments of the particles will align with the field, leading to a change in the overall magnetic properties of the particles. Recently, we found that besides the *in-situ* converted cobalt embedded carbon (Co@carbon) matrix on the bottom glass during laser direct writing [26], a thin layer of the ultrafine yet dense 3 nm Co NPs is attached on the confinement glass at the meantime. We assume that ultrafast laser-induced well-aligned uniform NPs could form strong photonic ‘hot spots’ and serve as plasmonic surfaces in many applications including SERS sensing. Herein, we further delve into formation of 2D plasmonic metasurfaces by utilizing the deposited high-dense ultrafine metal NP arrays on the top confinement glass, by MF assisted ultrafast laser direct deposition (MAPLD). During ultrafast laser irradiation, the laser plasma plume forms with high heat and pressure. The metal-organic-framework (MOF) materials are thus ablated, and converted by photochemical reactions within this plasma plume. In the meantime, the Co NPs and carbon species deposit on to the top confinement glass by ultrafast pulsed laser deposition mechanism, forming uniform C@carbon thin film. Tunable plasmonic patterns could be fancily written by a programmable scanning algorithm of the laser configurations and controllable hydrophobicity could be further designed by laser-induced dewetting (LDW) patterns, laser factors, and the involvement of MF. Ultrafine yet compact graphene-coated Co NPs are uniformly embedded in the carbon and provide superior plasmonic ‘hot spots’. SERS sensors are thus obtained without additional modification, while the bottom Co@carbon metamaterials are served as advanced catalyst for electrochemical water splitting. The ‘turn-waste-into-value’ concept utilized here not only satisfies the green chemistry standards, but also explores a new application of the surface residues. This customized SERS sensor from surface glass shows enhanced sensitivity, environmental adaptivity, and reusability, providing a promising green manufacturing technology for 2D plasmonic pattern fabrication on a large scale.

2. Results and discussion

The fabrication of the tunable plasmonic surface was shown in figure 1, and the detailed experimental description was provided in supporting information. The precursor preparation was as same as in our previous study [26]. In general, a ZIF-67/N-methyl-2-pyrrolidone slurry was coated on 9 μm copper foil and followed with drying at 100 °C for 12 h. The ZIF-67 coated copper foil was sandwiched by two pieces of glass slides and sealed tightly. An MF was introduced by placing a strong magnet down below the bottom glass and the ultrafast 5 ps laser treatment was applied from the upper confinement glass, as illustrated in figure 1(a). Other than the total screening of the whole ZIF-67 samples for graphene coated cobalt embedded carbon (G@Co@carbon) metamaterials, the scanning algorithm was also programmed to three different

pattern structures (PSz): honeycomb (HC), re-entrant honeycomb (RH), and chiral truss (CT) for different structural hydrophobicity purposes. A thin uniform ca. 50 μm thickness of G@Co@C patterns (figure 1(b)) was then deposited on the top confinement glass and was peeled off with washing and drying process. Figure 2 presented detailed SEM images of the top surface for the coated glass. In general, the involvement of MF generated a more uniform particle distribution together with the higher laser energy. Therefore, ultrafine yet compact Co NP arrays were obtained in these laser patterns under the guidance of MF manipulation, as shown in figure 1(c). The final products were named by their patterns with laser energy and MF existence, as PS-X or PS-XM. PS could be HC, RH, and CT while X stood for laser condition. Naming with M indicated the product was processed with MF involvement. For example, CT-1hM means a chiral truss plasmonic pattern processed by the highest laser energy under the MF. Full naming details are displayed in table S1.

In this report, the MAPLD could be closely related to the pulsed laser deposition (PLD) process, as demonstrated in figure 1(d) and the schematic comparison of PLD with MAPLD in figure S2. The ZIF-67 precursor and the top confinement glass could be treated as the target and the substrate in the PLD process, respectively. When the ultrafast 5 ps pulsed laser shot in and was absorbed by the ‘target’ ZIF-67, the laser energy was converted to electronic excitation and then into thermal, chemical, and mechanical energy. The MF further enhanced the phenomena and promoted the resulting evaporation, ablation, and exfoliation. Besides the *in-situ* conversion of Co/carbon metamaterials, the ejected Co NPs and carbon species in the plasma plume expanded onto the ‘PLD substrate’, the top confinement glass, forming thin films of Co NPs with carbon patterns. High resolution transmission electron microscope (HR-TEM) images again supported the importance of MF. Without MF, coarse G@Co NPs were observed (figure 1(e)). The MF successfully manipulated the Co NP formation and spatial arrangement, where dense and compact G@Co NPs were clearly seen in the HR-TEM images in figure 1(f). Figures 2(g) and (h) provided more HR-TEM images about PS-12M and PS-11M. The mechanism of MF-induced finer NPs is that the Co NPs are ‘cut’ by the MF and formed smaller sizes. Atomic force microscope (AFM) images in figures 2(i) and (j) gave surface structure details of the PS-h and PS-hM samples. The MF again took control over the Co NP formation and distribution for the surface morphology.

Compared with a typical PLD process where sophisticated sample/gas preparation, high-vacuum or inert atmosphere, long time, and high energy consumption were required, our MAPLD process was in one step, fast (5 cm \times 5 cm within 10 s), and was carried out in ambient conditions. Since the laser-converted ZIF-67 on the bottom glass was proven to be an excellent Co@C composite catalyst for electrochemical water-splitting, we extended the deposited Co@C on the upper glass with tunable pattern design for plasmonic applications for the maximization usage of precursor materials, which resulted in almost zero waste. This unique ultrafast laser deposition technique is not only eco-friendly but also takes full use of the precursors which could maximize the overall

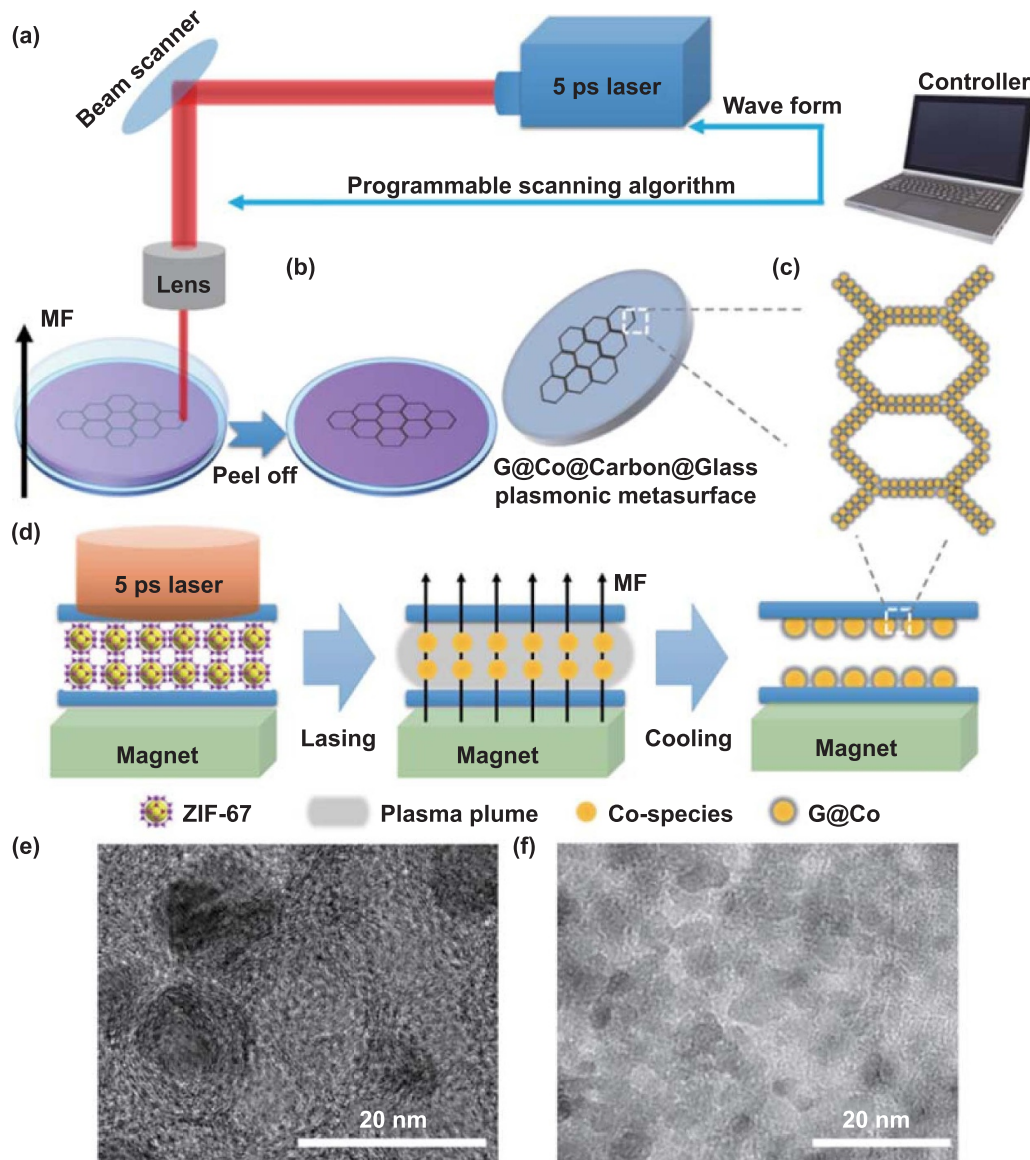


Figure 1. Fabrication of the tunable plasmonic surface by MAPLD. (a) Experimental setup for tunable MAPLD. (b) Top layer is collected as a plasmonic surface. (c) The extracted Co NPs are well-aligned by MF in the surface pattern. (d) Schematic illustration of the importance of MF during laser processing. HR-TEM images of (e) without MF and (f) with MF under high laser energy.

margin profit by getting two products from one single manufacturing process. The methodology used here might give a deeper insight into the fabrication process optimization and green manufacturing standards.

The particle movements with/without MF during the MAPLD process were simulated by COMSOL Multiphysics to investigate the MF-manipulated NP assembly mechanism, and the results were displayed in figure 3. In the case of ZIF-67 treatment without the application of an MF, the charged particles emitted following laser excitation exhibit unidirectional motion, ultimately resulting in their sparsely distributed deposition on the upper glass substrate. In contrast, the paramagnetic Co clusters, when subjected to the influence of the MF, undergo a controlled circular motion around the center of the laser spot. This manipulation of charged particles within the plasma plume leads to a reduction in the distance traveled by particles ejected with the same initial velocity,

resulting in a more compact and finely distributed deposition pattern on the upper glass substrate. For more comprehensive insights, detailed simulation procedures and outcomes are elaborated upon in the supporting information. Additionally, we have provided full-length videos in the supplementary information (videos S1 and S3), along with figure S3, which offer a closer examination of plasma expansion during the ultrafast LDW process, both from frontal and top perspectives. In these videos, the plasma plume originating from the laser spot displays a scattered pattern throughout space, resulting in a disorganized central-scattered plume. In contrast, the MAPLD process, as depicted in videos S2, S4, and figure S4, demonstrates a vertically oriented plasma plume movement, primarily driven by MF manipulation. Within this designated vertical plasma plume, Co and carbon species are more uniformly deposited on the upper glass substrate compared to scenarios without MF involvement. The MF-induced circular

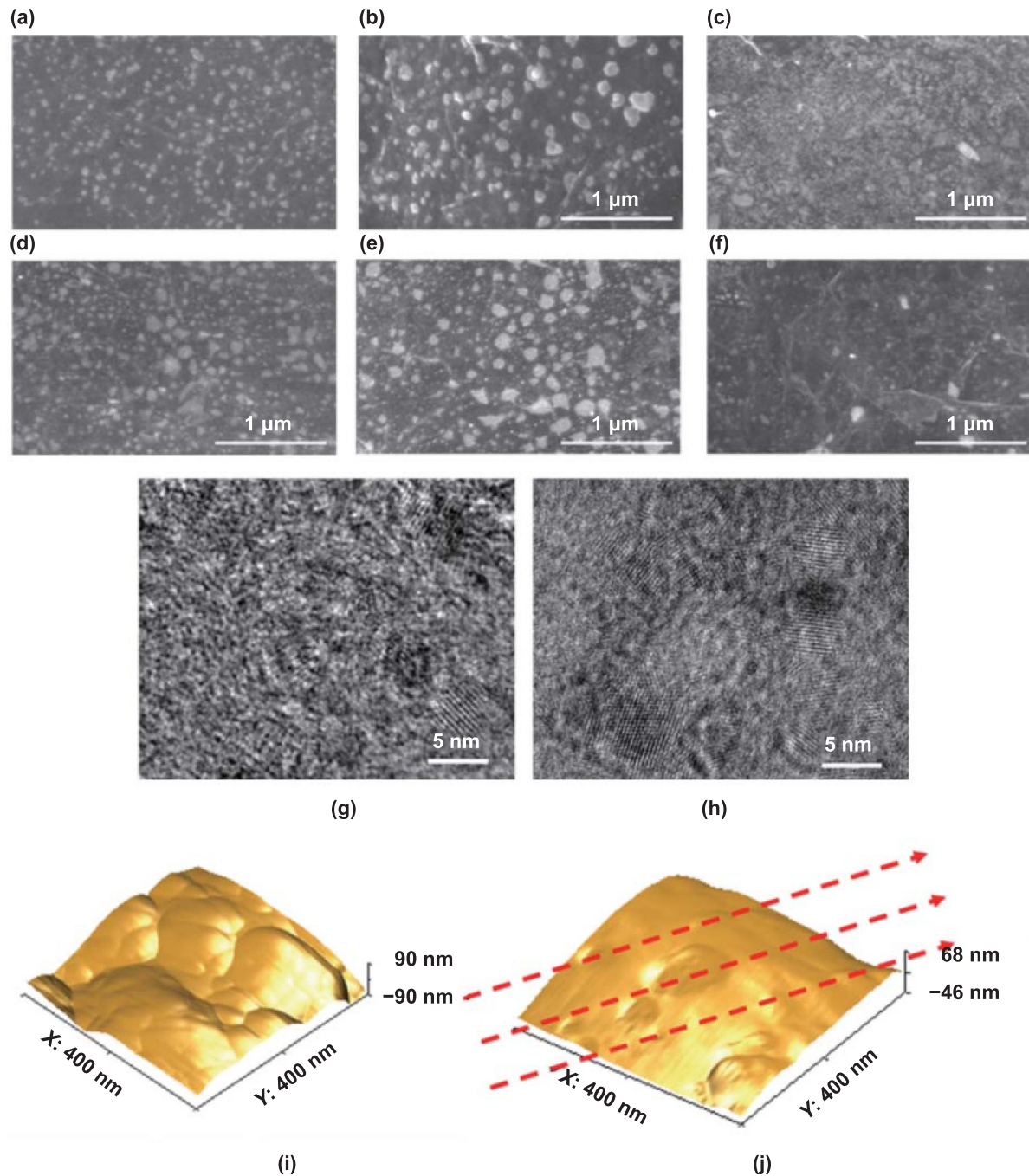


Figure 2. Microstructure characterization metal nanoparticles (NPs) after MAPLD and PLD without magnetic field (MF). SEM images of (a) PS-hM, (b) PS-mM, (c) PS-IM and their counterpart without MF: (d) PS-h, (e) PS-m, and (f) PS-l; HR-TEM images of (g) PS-mM and (h) PS-IM; AFM images of (i) PS-h and (j) PS-hM.

movement effectively repositions the Co NPs into a finer and more compact assembly. This refined assembly configuration provides a greater density of plasmonic ‘hot spots,’ which, in turn, enhances SERS sensitivity compared to situations where MF manipulation is absent.

To investigate the optical mechanisms behind the graphene-coated Co NPs, finite-difference time-domain (FDTD) simulations were carried out using FDTD Solutions software (Lumerical Co. Ltd). Detailed simulation setups are provided in supporting information. Figures 4(a) and (b) were the proposed model for PS-h, PS-hM, and their

corresponding electric field (EF) enhancements were calculated in figures 4(c) and (d), respectively. According to the HR-TEM results, the PS-h was set as three-coarse G@Co NPs with sizes of 5, 10, and 15 nm, and the PS-hM was set as aligned 3×4 G@Co NP arrays with uniform sizes of 3 nm. The normalized EF intensity distributions in the x - y planes of PS-h were around two times lower than that of the PS-hM, as the max EF intensity is 1.6 and 3.3 for PS-h and PS-hM, respectively. High EF intensity, as the ‘hot spots’ in the red bar, was rarely seen in PS-13 because of the coarse Co NPs. The MF-aligned uniform Co NPs in PS-hM, however,

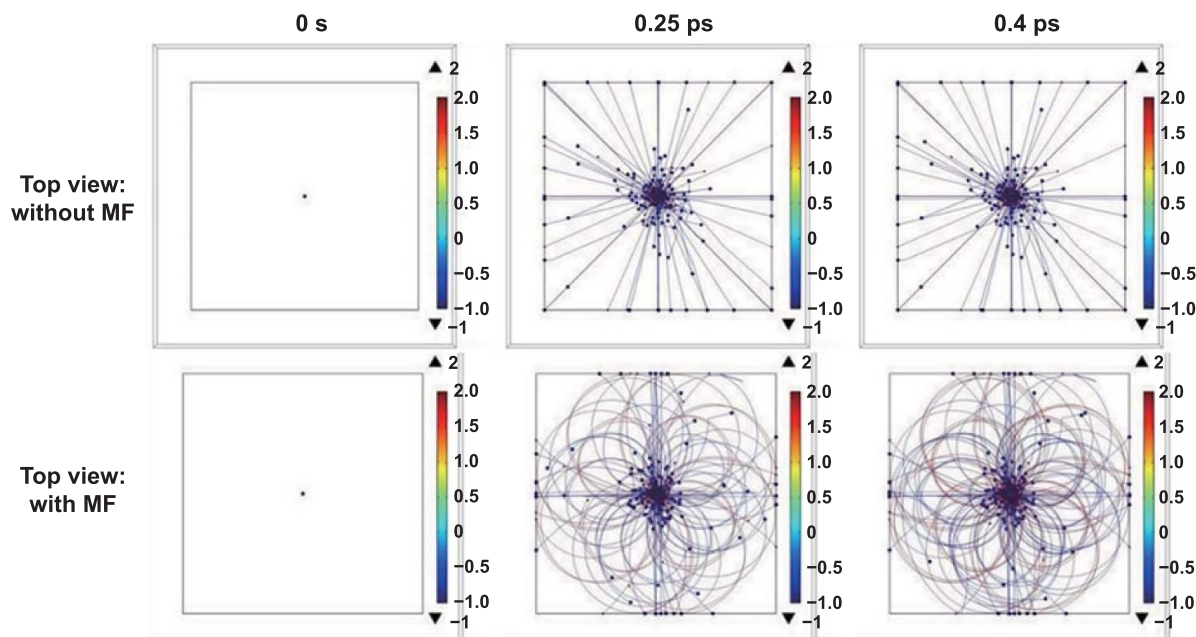


Figure 3. Top view of simulated particle movements with/without MF under different time scale.

provided abundant ‘hot spots’ at the intersections of Co NPs due to the enhanced plasmonic effects of ordered metal NP assembly [14, 18, 25]. This as-synthesized uniform, reliably and stable metasurface is critical for practical application of SERS substrates.

Figures 4(e) and (f) provided the SERS spectra of 10^{-10} mol l^{-1} (M) RhB aqueous solution loaded PS samples without MF and with MF, respectively. The black baseline was the bare sample, 10^{-8} M RhB loaded on glass. All metasurfaces showed enhanced Raman signals for the detection of RhB with a relatively low concentration of 10^{-8} M, and PS-M samples with much higher enhancements. One of the signal peaks of RhB, 1649 cm^{-1} , was selected to better understand the influence of laser energy and MF involvement. Figure S5 plotted the SERS intensities at 1649 cm^{-1} of all PS samples and their corresponding Raman intensity/RhB ratio. Higher laser energy density and the existence of MF could contribute to higher SERS signal enhancements. PS-hM had the highest SERS signals, which was an 18 fold increment compared to bare RhB and almost a two-fold increment compared to PS-h, the sample without MF but under the same laser conditions. A brief schematic of the reason for SERS enhancement was described in figure S6. The MF-manipulated ultrafine yet compact NPs were crucial to introducing active sites for plasmonic applications and the SERS mapping was carried out to examine their uniformity. Figure S7 presented the SERS signals at 1649 cm^{-1} of MF-manipulated metasurfaces and figure S8 for metasurfaces without MF, countering the bare RhB sample. Weak RhB signals could be detected in the bare RhB@Glass sample while all RhB@PS-M samples were ‘hot’ with RhB signals. Regular PS sample still showed decent SERS enhancement, especially when the laser energy is high at PS-h. Overall, these findings fitted well with our previous assumptions and FDTD simulations: higher laser energy and MF manipulation would lead to finer and denser Co NPs,

and these well-aligned compact NP arrays could significantly enhance the plasmonic ‘hot spot’ that could benefit a lot of plasmonic devices like SERS sensors. In addition, we have conducted measurements of the absorption spectrum under different processing conditions using a spectrum photometer (figure S9). Our results clearly demonstrate that the absorption of the Co NP-based platform is substantially lower under conditions without the application of an MF, specifically in cases PS-11 and PS-12. These findings strongly corroborate the notion that the presence of an MF significantly enhances the optical absorption characteristics of the plasmonic platform. Consequently, this enhancement contributes to an improved surface plasmonic resonance, which is pivotal for optimizing the performance of SERS.

The low optical absorption of Co NPs at 633 nm , a wavelength commonly used in SERS, is noteworthy. This study explores a novel aspect of SERS by investigating the SERS performance of the graphene/Co structure under an MF, which reveals a significantly higher enhancement compared to non-MF conditions, primarily due to the unique nanostructure after MAPLD. This nanostructure features an ultrahigh density of uniformly distributed metal particles with ultrasmall gaps between them. While materials like Co are not typically considered ideal for traditional SERS due to their low optical absorption, the application of an MF-controlled laser processing in MAPLD overcomes this limitation, resulting in a highly sensitive SERS substrate. This underscores the potential utility of Co NPs within a specific context. Moreover, our study seeks to explore alternative materials for SERS beyond traditional Ag and Au NPs, which is much more expensive than earth abundant materials such as Co. It is important to note that Co NPs represent just one selection and may not be universally ideal for SERS. Our platform holds applicability to a variety of metals and alloys that may offer superior SERS performance compared to Co. In addition, the enhancement

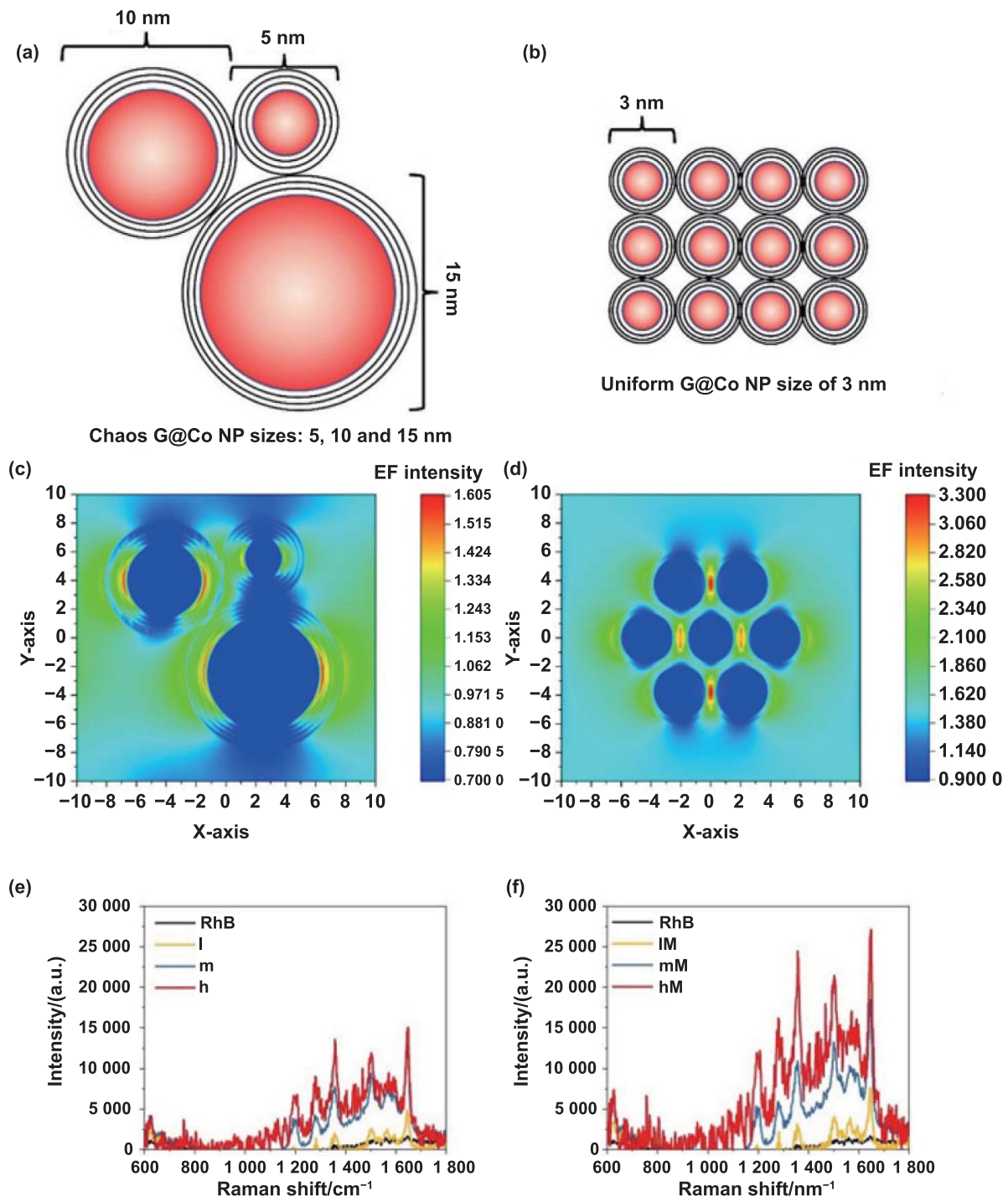
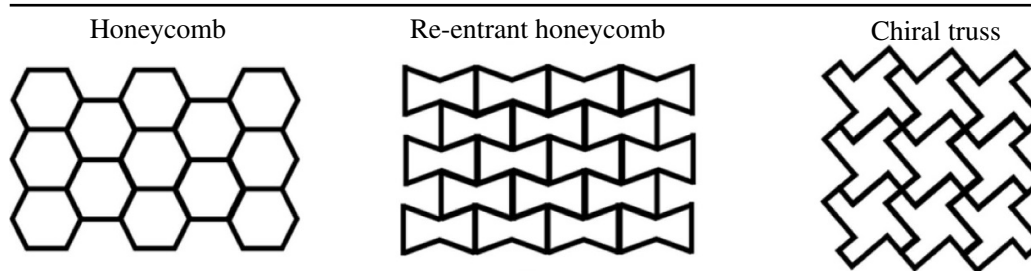


Figure 4. Finite-difference time-domain (FDTD) simulations for optical property of graphene-coated metal NPs. Model setup for (a) PS-h and (b) PS-hM and their simulated corresponding electric field intensity distribution in the X–Y plane in (c) and (d), respectively. SERS spectra of RhB-loaded plasmonic surfaces: (e) without MF and (f) with MF.

of Raman scattering can be significantly attributed to the graphene coating on the Co NPs. It is important to note that in both scenarios, whether an MF is applied or not, the Co NPs consistently feature a graphene coating, highlighting the magnetically induced nanostructure as the key factor in the observed SERS enhancement. This exceptional nanostructure leads to a remarkable SERS enhancement, exceeding 18 times, largely influenced by the presence of an MF.

Another key feature of laser processing is the ability to program the scanning algorithms and the adaptability to precisely switch laser conditions during laser irradiation. Since different laser conditions and the MF involvement have proven to be direct factors that could regulate and control the final products' SERS performance, the SERS signals for the intersection of two different metasurfaces were studied to better design the hybrid metasurface structures. As shown in figure S9, three

Table 1. Water contact angles of the plasmonic surfaces. The HC, RH, and CT patterns are shown in the upper section.


Patterns	Contact angle	Patterns with MF	Contact angle
HC-11	33.7°	HC-11M	38.4°
RH-11	20.3°	RH-11M	47.9°
CT-11	11.9°	CT-11M	38.5°
HC-12	29.8°	HC-12M	40.9°
RH-12	21.0°	RH-12M	38.8°
CT-12	20.2°	CT-12M	35.5°
HC-13	36.2°	HC-13M	36.8°
RH-13	35.6°	RH-13M	39.6°
CT-13	26.3°	CT-13M	30.8°

vertical lines were plasmonic patterns lased from low to high energy without MF. Three lateral lines were plasmonic patterns lased from low to high energy with MF, marked as IM, mM, and hM, respectively. The six lines were then loaded with 10^{-10} M RhB as SERS sensors and the intersections of each two lines were studied by Raman SERS mapping. Figures S9(b)–(j) were SERS intensities at 1649 cm^{-1} of the intersections of hM-h, hM-m, hM-l; mM-h, mM-m, mM-l; and IM-h, IM-m, IM-l, respectively. A clear boundary could be seen for hM-l, mM-l, and IM-l, presenting the importance of laser energy and MF manipulation of Co NPs. Only under the MF influence, the orientation of NPs could be controlled in the carbon matrix to the well-aligned NP arrays. The NPs, which have a net magnetic moment due to their magnetic anisotropy, align themselves with the MF, resulting in an anisotropic distribution of NPs within the carbon matrix. The desirable plasmonic platform was then produced under the highest laser input with MF.

Nevertheless, a major problem is reproducibility: often the SERS signal differs among different nanostructures (or locations on the support) due to variation in morphologies of nanostructures [27–29]. Besides, the SERS enhancements are not uniform in real samples, and only a few sites exhibit the highest SERS enhancement. On the other hand, only molecules located (usually $<2\text{ nm}$) within the ‘hot spots’ could contribute to the overall SERS signals. Therefore, both (1) the uniformity of hot spots on backbone patterns and (2) the well distribution of molecules on these corresponding ‘hot spots’ are necessary to achieve high-sensitive and reliable plasmonic surfaces.

With these findings in mind, we started the customization of metasurface structures, and the relationship between

three surface patterns: HC, RH and CT, and their hydrophobicity were studied. Detailed water contact angle photos were available in supporting information, from figures S10–S12, and their water contact angles were calculated and presented in table 1. Generally, CT structures had the lowest water contact angles which mean more hydrophilic, and HC structures tended to be more hydrophobic. RH structures sit in the middle of CT and HC structures. Furthermore, higher laser energy also increased their hydrophobicity, mainly due to higher graphitic crystallinity in the carbon backbone which is highly hydrophobic. From regular SERS testing results, higher laser energy and MF-manipulation could achieve better SERS enhancements, like PS-hM. However, combining the results from SERS and water contact angle measurements, PS-hM might not be an ideal candidate for aqueous solution-based SERS sensing because of the uneven loading of active materials. Special attention should be given, and designated solutions were needed to overcome this issue.

A multi-scale engineered hybrid SERS pattern design was developed to empower the best SERS sensing platform, PS-hM, with customized hydrophilicity. Owing to the flexibility of laser processing features, the laser power could be precisely controlled during each step of the process. Herein, we proposed a two-scale hybrid SERS pattern by combing the most SERS sensing PS-hM and the most hydrophilic PS-l, together with the aforementioned three metastructures: HC, RH, and CT. As shown in figures 5(a)–(c), the SERS patterns were divided into two parts: lateral scanning and vertical scanning for the scanning algorithm. One side of the scanning was conducted by high laser energy, with MF, serving as the SERS sensing platform. The other side of the scanning was laser processed by low laser energy without MF, aiming to

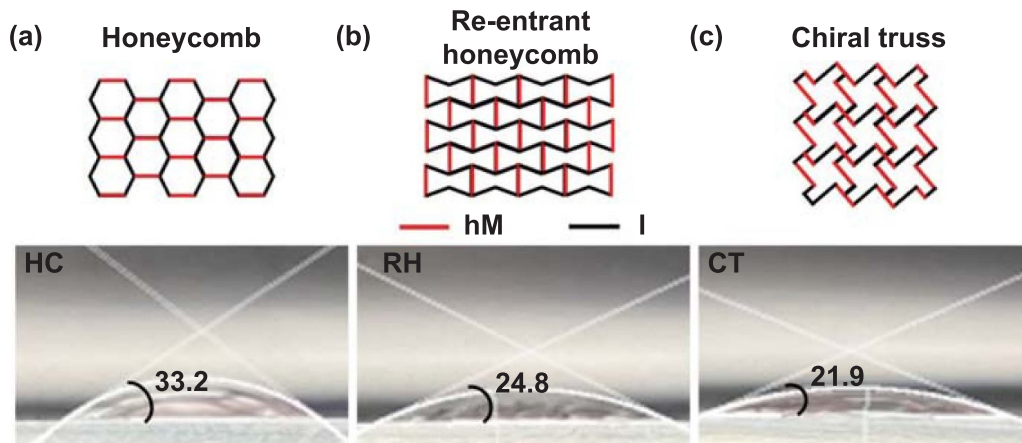


Figure 5. Water contact angles of various multi-scale engineered hybrid metasurfaces. (a) HC-hM/I, (b) RH-hM/I, and (c) CT-hM/I.

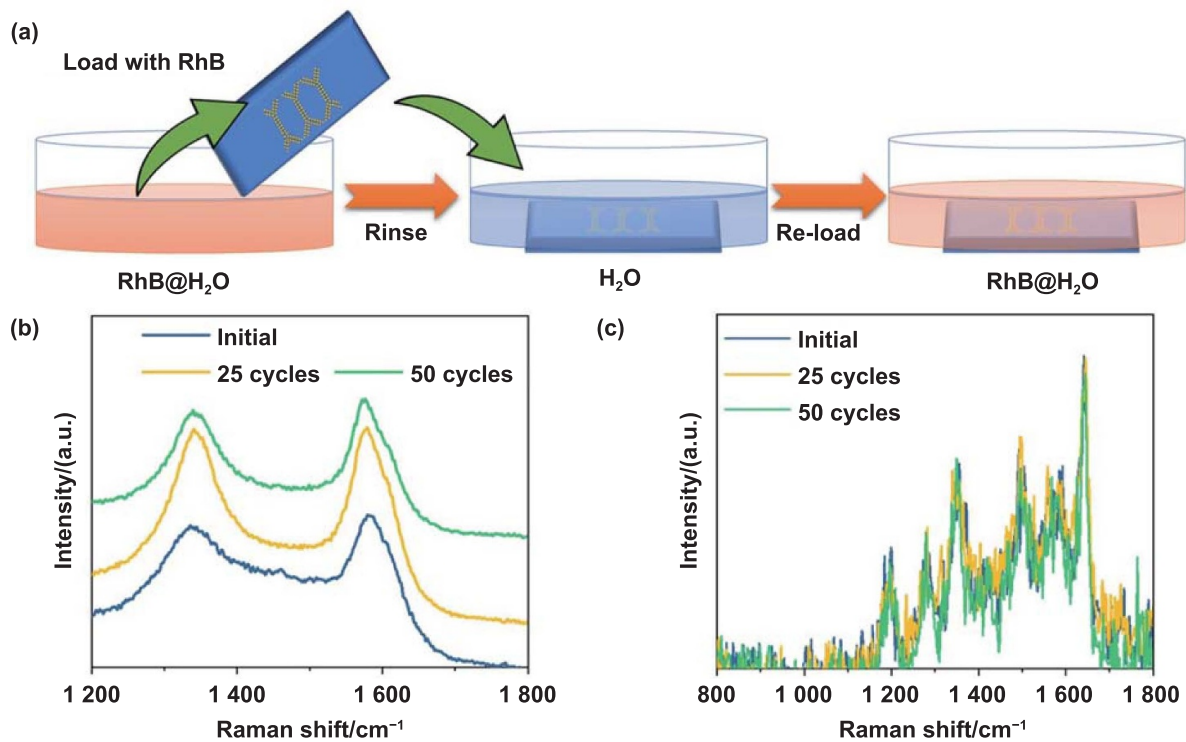


Figure 6. Reusable testing of CT-hM/I. (a) The schematic of the RhB rinsing process. (b) Raman spectra for the rinsed CT-hM/I after 25 and 50 cycles. (c) SERS signals for the RhB re-loaded CT-hM/I after 25 and 50 cycles.

adjust the hydrophobicity of overall metasurface patterns. The pristine water contact angles for HC-hM, RH-hM, and CT-hM were 36.8° , 39.6° , and 30.8° , respectively. After the multi-scale engineering design, the water contact angles were regulated to 33.2° , 24.8° , and 21.9° , respectively. The angles were reduced by 9.8%, 37.4%, and 28.9% for HC, RH, and CT, respectively. This multi-scale engineering design successively regulated the hydrophobicity by adjusting the water contact angles from 20° to 40° , with the combination of three pattern designs by one-step MAPLD in air. With the help of improved hydrophilicity, the Raman spectra were taken back to check the potential loss of SERS sensitivities.

The reusability of the SERS sensing platform remains one of the key issues that prevent its widespread applications.

Typically, SERS sensors are delicately fabricated by assembling metal NPs with supporting substrates like graphene or other 2D materials. Such composite systems are usually fragile and could only be loaded with sensing objectives once because the delicate structures might be reformed after rinsing by breaking the weak van der Waals force. Our MAPLD provided an ultimate solution to reuse the plasmonic metasurfaces as the Co NPs were tightly deposited on the glass substrate and were further 'glued' by the graphene coating, as the result of similar PLD mechanism. The as-tested RhB-loaded CT-hM/I was chosen to perform the cyclability for it is superior water wettability. As shown in figure 6(a), the CT-hM/I was first loaded with RhB, followed by initial SERS sensing tests. The RhB-loaded CT-hM/I was then rinsed with water

to remove RhB. Raman spectra were carried out to examine the metasurface integrity of the rinsed CT-hM/I at this step, presented in figure 6(b). The rinsed CT-hM/I was then re-loaded with RhB for the second cycle, and the process was repeated 50 times and the 25th and 50th SERS signals were given in figure 6(c). From figure 6(b), the D/G peak ratio of carbon materials remains unchanging, stating the rinsing process was damage-free and the CT-hM/I was super stable and robust [30–32]. The 25th and 50th cycle's SERS signals in figure 6(c) also remained similar and this well supported the reusability of our robust plasmonic patterns.

3. Conclusion

In conclusion, we demonstrated scalable manufacturing of tunable plasmonic patterns by the MF manipulated ultrafast laser direct writing in air. Under the MF manipulation, the growth of the extracted Co clusters was terminated once reached their critical magnetic size of 3 nm. Afterward, the 3 nm ultrafine Co NPs were aligned by MF in spatial distribution for forming a dense compact in the carbon matrix on the top glass as robust plasmonic 'hot spots'. The laser scanning algorithm, laser conditions, and the MF involvements were introduced as three major factors to design the multi-scale hybrid plasmonic platform. Firstly, single-scale plasmonic surfaces were loaded with RhB as SERS sensors to explore their plasmonic performances. Secondly, water contact angle tests were carried out to derive the relationship between hydrophobicity and plasmonic enhancement of these metasurfaces. Thirdly, the most plasmonic sensitive PS-hM and the most hydrophilic PS-I were integrated via a two-scale engineered hybrid design by splitting the whole laser scanning algorithm into two parts. The resultant hybrid CT-hM/I system presented adjustable hydrophobicity which could be served in various detection environments. Finally, the hybrid SERS platform, CT-hM/I was rinsed and re-loaded with RhB for 50 cycles, and its SERS performance remained unchanging, proofing to be a reusable yet robust SERS sensor. Overall, our tunable MAPLD in air meets the green manufacturing criteria and turns 'waste' into 'value'. The as-synthesized multi-scale hybrid plasmonic platform shows customized hydrophobicity and plasmonic 'hot spots', owing to the feasibility of laser processing and MF-manipulation. The plasmonic resonance effect in SERS sensors is directly linked to the significant energy enhancement observed in the Raman scattering signal. By harnessing the unique capabilities of plasmonic nanostructures to generate intense local electro MFs, SERS has become a powerful analytical tool with widespread applications in diverse fields due to its exceptional sensitivity and selectivity. The remarkable outcomes witnessed in SERS sensors underscore the vast potential of this technology in driving energy-related applications toward a sustainable and cleaner future. Its transformative capabilities extend to diverse fields, such as photocatalysis, photovoltaics, and clean water, offering promising avenues for efficient and environmentally friendly energy solutions.

Acknowledgments

G J C acknowledges the support by the Office of Naval Research's NEPTUNE Program under the Grant Number N00014-16-1-3109, and the National Science Foundation CMMI NanoManufacturing Program.

ORCID iD

Gary J Cheng  <https://orcid.org/0000-0002-1184-2946>

References

- [1] Kang E S H, Chaharsoughi M S, Rossi S and Jonsson M P 2019 Hybrid plasmonic metasurfaces *J. Appl. Phys.* **126** 140901
- [2] Hu J, Bandyopadhyay S, Liu Y H and Shao L Y 2021 A review on metasurface: from principle to smart metadevices *Front. Phys.* **8** 586087
- [3] Lin D M, Fan P Y, Hasman E and Brongersma M L 2014 Dielectric gradient metasurface optical elements *Science* **345** 298–302
- [4] Watts C M, Liu X L and Padilla W J 2012 Metamaterial electromagnetic wave absorbers *Adv. Mater.* **24** OP98–120
- [5] Lee N, Yoon B, Kim T, Bae J Y, Lim J S, Chang I and Cho H H 2020 Multiple resonance metamaterial emitter for deception of infrared emission with enhanced energy dissipation *ACS Appl. Mater. Interfaces* **12** 8862–9
- [6] Arbabi A, Horie Y, Bagheri M and Faraon A 2015 Dielectric metasurfaces for complete control of phase and polarization with subwavelength spatial resolution and high transmission *Nat. Nanotechnol.* **10** 937–43
- [7] Yifat Y, Eitan M, Iluz Z, Hanein Y, Boag A and Scheuer J 2014 Highly efficient and broadband wide-angle holography using patch-dipole nanoantenna reflectarrays *Nano Lett.* **14** 2485–90
- [8] Losurdo M, Bergmair I, Dastmalchi B, Kim T H, Giangregorio M M, Jiao W Y, Bianco G V, Brown A S, Hingerl K and Bruno G 2014 Graphene as an electron shuttle for silver deoxidation: removing a key barrier to plasmonics and metamaterials for SERS in the visible *Adv. Funct. Mater.* **24** 1864–78
- [9] Yang K, Wang J Y, Yao X, Lyu D, Zhu J F, Yang Z L, Liu B W and Ren B 2021 Large-area plasmonic metamaterial with thickness-dependent absorption *Adv. Opt. Mater.* **9** 2001375
- [10] Favron A, Goudreau F A, Gosselin V, Groulx J, Côté M, Leonelli R, Germain J F, Phaneuf-L'Heureux A L, Francoeur S and Martel R 2018 Second-order raman scattering in exfoliated black phosphorus *Nano Lett.* **18** 1018–27
- [11] Wu J B, Lin M L, Cong X, Liu H N and Tan P H 2018 Raman spectroscopy of graphene-based materials and its applications in related devices *Chem. Soc. Rev.* **47** 1822–73
- [12] Verzhbitskiy I A et al 2016 Raman fingerprints of atomically precise graphene nanoribbons *Nano Lett.* **16** 3442–7
- [13] Ferrari A C and Basko D M 2013 Raman spectroscopy as a versatile tool for studying the properties of graphene *Nat. Nanotechnol.* **8** 235–46
- [14] Shen W et al 2015 Reliable quantitative SERS analysis facilitated by core-shell nanoparticles with embedded internal standards *Angew. Chem., Int. Ed. Engl.* **54** 7308–12
- [15] Zhao Y, Chen G X, Du Y X, Xu J, Wu S L, Qu Y and Zhu Y W 2014 Plasmonic-enhanced Raman scattering of graphene on growth substrates and its application in SERS *Nanoscale* **6** 13754–60

- [16] Jiang H Q, Jin S Y, Wang C, Ma R Q, Song Y Y, Gao M Y, Liu X T, Shen A G, Cheng G J and Deng H X 2019 Nanoscale laser metallurgy and patterning in air using MOFs *J. Am. Chem. Soc.* **141** 5481–9
- [17] Kneipp K, Moskovits M and Kneipp H 2006 *Surface-Enhanced Raman Scattering: Physics and Applications* (Springer)
- [18] Stoerzinger K A, Lin J Y and Odom T W 2011 Nanoparticle SERS substrates with 3D Raman-active volumes *Chem. Sci.* **2** 1435–9
- [19] Jin S Y, Wang Y X, Motlag M, Gao S J, Xu J, Nian Q, Wu W Z and Cheng G J 2018 Large-area direct laser-shock imprinting of a 3D biomimic hierarchical metal surface for triboelectric nanogenerators *Adv. Mater.* **30** 1705840
- [20] Gao H, Hu Y W, Xuan Y, Li J, Yang Y L, Martinez R V, Li C Y, Luo J, Qi M H and Cheng G J 2014 Large-scale nanoshaping of ultrasmooth 3D crystalline metallic structures *Science* **346** 1352–6
- [21] An L C, Jiang H Q, Branco D D C, Liu X T, Xu J and Cheng G J 2022 Self-packaged high-resolution liquid metal nano-patterns *Matter* **5** 1016–30
- [22] Jiang H, Liu X T, Zhu M N, Xu J, An L C, Sui P F, Luo J L and Cheng G J 2022 Nanoalloy libraries from laser-induced thermionic emission reduction *Sci. Adv.* **8** eabm6541
- [23] Jiang H Q, Tong L, Liu H D, Xu J, Jin S Y, Wang C, Hu X J, Ye L, Deng H X and Cheng G J 2020 Graphene-metal-metastructure monolith via laser shock-induced thermochemical stitching of MOF crystals *Matter* **2** 1535–49
- [24] Graham D, Moskovits M and Tian Z Q 2017 SERS—facts, figures and the future *Chem. Soc. Rev.* **46** 3864–5
- [25] Chen H Y, Lin M H, Wang C Y, Chang Y M and Gwo S 2015 Large-scale hot spot engineering for quantitative SERS at the single-molecule scale *J. Am. Chem. Soc.* **137** 13698–705
- [26] Xu J, Wang R X, Jiang H Q, Liu X T, An L C, Jin S Y, Deng B W, Wu W Z and Cheng G J 2021 Magnetically aligned ultrafine cobalt embedded 3D porous carbon metamaterial by one-step ultrafast laser direct writing *Adv. Sci.* **8** 2102477
- [27] Le Ru E C, Meyer M, Blackie E and Etchegoin P G 2008 Advanced aspects of electromagnetic SERS enhancement factors at a hot spot *J. Raman Spectrosc.* **39** 1127–34
- [28] Willets K A 2014 Super-resolution imaging of SERS hot spots *Chem. Soc. Rev.* **43** 3854–64
- [29] Kleinman S L, Frontiera R R, Henry A I, Dieringer J A and Van Duyne R P 2013 Creating, characterizing, and controlling chemistry with SERS hot spots *Phys. Chem. Chem. Phys.* **15** 21–36
- [30] Sun X M, Ye J L, Pan F, Xu J, Cheng T, Wang X Y, Ikram M and Zhu Y W 2018 Hierarchical porous carbon obtained from frozen tofu for efficient energy storage *New J. Chem.* **42** 12421–8
- [31] Cheng T et al 2018 A spray-freezing approach to reduced graphene oxide/MoS₂ hybrids for superior energy storage *Energy Storage Mater.* **10** 282–90
- [32] Xu J et al 2016 A hierarchical carbon derived from sponge-templated activation of graphene oxide for high-performance supercapacitor electrodes *Adv. Mater.* **28** 5222–8